Letter

Prediction of hot zone-center optical phonons in laser-irradiated molybdenum disulfide with a semiconductor multitemperature model

Zherui Han [1], Peter Sokalski [2], Li Shi [2], and Xiulin Ruan [1,*]

[1] *School of Mechanical Engineering and the Birck Nanotechnology Center, Purdue University, West Lafayette, Indiana 47907-2088, USA*

[2] *Walker Department of Mechanical Engineering, The University of Texas at Austin, Austin, Texas 78712, USA*

(Received 1 August 2022; revised 4 January 2023; accepted 10 January 2023; published 23 January 2023)

A previous multitemperature model (MTM) resolving phonon temperatures at the polarization level and measurements have uncovered remarkable nonequilibrium among different phonon polarizations in laser-irradiated graphene and metals. Here, we develop a semiconductor-specific MTM (SC-MTM) by including electron-hole pair generation, diffusion, and recombination, and show that a phonon polarization-level model does not yield observable polarization-based nonequilibrium in laser-irradiated molybdenum disulfide (MoS_2). In contrast, appreciable nonequilibrium is predicted between zone-center optical phonons and the other modes. The momentum-based nonequilibrium ratio is found to increase with decreasing laser spot size and interaction with a substrate. This finding is relevant to the understanding of the energy relaxation process in two-dimensional optoelectronic devices and Raman measurements of thermal transport.

DOI: 10.1103/PhysRevB.107.L041407

The thermal relaxation of nonequilibrium charge and energy carriers is essential in operating semiconductor devices and laser processing of metals [1,2]. The energy cascade in such a process is usually described as a hierarchical energy flow from an electrical or optical excitation to hot electrons, which are then coupled to optical phonons and finally decayed into the lattice. The efficiency of optoelectronic devices is increased by the so-called "phonon bottleneck" [3–5] associated with the coupling between the hot electrons and phonons. This effect has been captured in a previous two-temperature model (TTM) and its refined successors [1,2,6–8] by assigning lumped temperatures to individual carrier subgroups. The TTM is also extended to consider semiconductors under photoexcitations [9]. Recent studies on the thermalization of the lattice reveal that the nonequilibrium between the optical and acoustical phonon polarizations and that among different acoustical phonon polarizations can be even more pronounced than that between electrons and phonons [10,11]. The nonequilibrium inside the lattice phonon bath can give rise to nonthermal melting in devices [12] and an inaccurate interpretation of thermal conductivity measurement based on Raman thermometry [10]. Past works have considered nonequilibrium between phonons with different frequency ranges or at different polarizations in the multitemperature model (MTM) [10,13] and the nonthermal lattice model (NLM) [14] that assign different temperatures to each phonon polarization or divide the phonons into low-frequency and high-frequency groups [15]. A polarization-based nonequilibrium has been considered in past studies of graphene [10,11,13] as well as a recent study of thin-film molybdenum disulfide (MoS_2) [16].

The polarization-based nonequilibrium is a result of different coupling strengths between the hot electrons and different phonon polarizations, such as the three different acoustic phonon branches in a simple metal [14]. In addition, the out-of-plane polarized flexural (ZA) phonons in monolayer graphene show a peculiar quadratic dispersion that is subject to an additional restrictive electron-phonon scattering selection rule compared to that for the other two linear acoustic dispersions [13]. Meanwhile, the size confinement effects on in-plane phonons in nanosized graphene can modify the coupling strength between different phonon polarizations [15].

In this Letter, we search for potential phonon nonequilibrium in MoS_2 thin films irradiated by a focused laser beam. The usual separation approach based on phonon energies or branches did not yield apparent nonequilibrium. Instead, we find that the zone-center optical phonons are hot by separation of phonons in both the energy and momentum spaces in our first-principles calculations of electron-phonon and phonon-phonon couplings. The calculated degree of nonequilibrium under the same experimental setup agrees well with a concurrent Raman experiment that reports a moderate nonequilibrium [17]. The zone-center optical phonon temperature exceeds those of the other phonon modes increasingly at a reduced laser spot size and by enhanced cooling of the other modes via an interface interaction between the MoS_2 thin layer and a substrate. While a prior study [8] has examined momentum-dependent electron-phonon coupling in multilayer tungsten diselenide (WSe_2) irradiated by ultrafast optical pulses, our results reveal that momentum-dependent electron-phonon and phonon-phonon coupling results in hot nonequilibrium phonons in both the energy and momentum spaces. Compared to recent theoretical predictions of zone-center and zone-boundary hot optical phonons in monolayer MoS_2 [18] and MgB_2 [19] during ultrafast pump-probe measurements, our theoretical calculation reveals zone-center hot optical phonons even in relatively thick MoS_2 flakes under steady-state focused laser heating and explains the finding

*ruan@purdue.edu

from a concurrent Raman measurement [17]. The current model has not considered excitons formed as bound electron-hole pairs, where the electrons are below the conduction band, and the holes are above the valence bands. The exciton binding energy of bulk MoS_2 might be close to room temperature. If we focus on a lattice temperature well above the room temperature with a high enough laser power, the thermal energy is higher than the exciton binding energy to break them into free electrons and holes in the conduction band and valence band, which are modeled here.

Unlike metals, laser irradiation of semiconductors would create electron-hole pairs, which subsequently undergo hierarchical energy relaxation in time and/or spatial scales [9,22]: quick thermalization of electrons (holes) by internal collisions, further energy relaxation by the emission of phonons, and eventual energy decay by an electron-hole recombination process. These processes are shown in Fig. 1(a) where we mark these relaxation processes onto a calculated band structure. In the case of strong laser excitation, electrons and holes can be separated to have different temperatures and warrant separate treatment [23]. Figure 1(b) shows the energy dissipation through electron- (hole-)phonon interactions (EPIs) and subsequent phonon-phonon scattering. Some phonon polarizations, usually the optical phonons, receive the majority of the dissipated energy and become overpopulated. The excess heat is then lost to the other phonon modes through phonon-phonon scatterings, including three-phonon and four-phonon processes. For a thin-film material supported by a substrate, phonon-mediated heat transfer across the interface gives rise to an interfacial thermal conductance (G_i). Besides mode-dependent electron-phonon and phonon-phonon couplings in the thin layers, mode-dependent phonon coupling across the interface with the substrate phonons, usually characterized by a large interface transmission coefficient for low-frequency acoustic vibrational modes [24], is another mechanism that can give rise to nonequilibrium among different phonon modes in the thin layer.

Our first-principles calculations are performed in the framework of density functional theory (DFT) as implemented in the Vienna *ab initio* simulation package (VASP) [25] and we obtain the phononic structure using density functional perturbation theory (DFPT) [26]. Interatomic force constants are calculated using the finite-difference method [27]. Phonon-phonon coupling strength is then calculated using a package developed by some authors of the present work, FOURPHONON [28]. We use QUANTUM ESPRESSO [29] along with a modified EPW package [30] to calculate the electron-phonon coupling strength and further the electron scattering rates due to phonons. In this framework, the coupling strength for a certain phonon mode ($\mathbf{q}$) is computed as $\lambda_{\mathbf{q}} = \frac{1}{N_F \omega_{\mathbf{q}}} \sum_{\mathbf{k},\mathbf{k}'} |g^{\mathbf{q}}_{\mathbf{k},\mathbf{k}'}|^2 \delta_{\mathbf{k}} \delta_{\mathbf{k}'+\mathbf{q}}$ [30], where $|g^{\mathbf{q}}_{\mathbf{k},\mathbf{k}'}|$ is the electron-phonon coupling matrix element involving electronic state $|\mathbf{k}\rangle$, $|\mathbf{k}'+\mathbf{q}\rangle$ and phonon mode $|\mathbf{q}\rangle$ with frequency $\omega_{\mathbf{q}}$, δ is the Dirac delta function, and N_F is the density of states. Further details on first-principles calculations are presented in the Supplemental Material [31].

An important question is how we should partition and regroup the energy carriers to represent the aforementioned origins of nonequilibrium phonons. For simplicity, we first consider a suspended sample and set $G_i = 0$ to examine the effects of mode-dependent electron-phonon and phonon-phonon coupling. We perform first-principles calculations to find spectral EPI and phonon scatterings. Figure 2 shows our calculated modewise electron-phonon scattering and phonon-phonon scattering strengths that are mapped onto phonon dispersions in bulk MoS_2. We observe from Fig. 2(a) that electrons are mainly coupled with zone-center phonons and the coupling strength ($\lambda_{\mathbf{q}}$) for a certain mode specified by its momentum ($\mathbf{q}$) shows a strong dependence on the wave vector for each phonon branch. Additionally, some optical phonons with low frequencies and near the zone center still show strong coupling with electrons. This feature implies that grouping phonons only by their energy range or phonon branches may

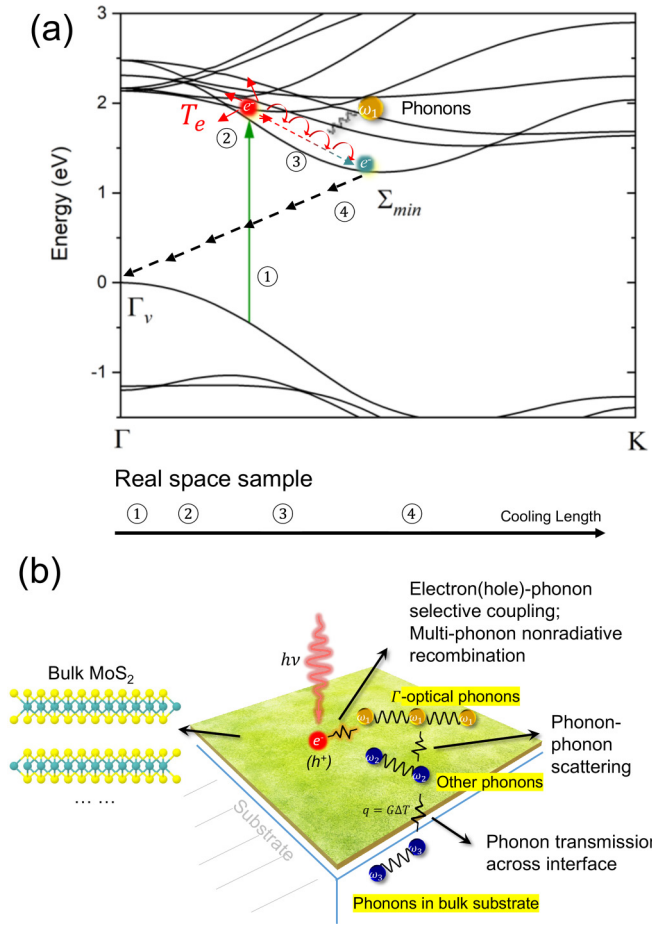

FIG. 1. Schematic of energy pathway in localized laser heating on bulk MoS_2. (a) Hot electron relaxation with different mechanisms mapped onto the calculated band structure of bulk MoS_2: ① photoexcitation, ② electron collisons, ③ electron-phonon coupling, and ④ multiphonon recombination. In this plot, Γ_v represents the valence band maximum and $\Sigma_{\min}$ represents the conduction band minimum. The bottom real space illustration represents the associated different cooling lengths in the spatial domain. (b) Schematic showing the energy transfer in electron-phonon coupling ③ and subsequent phonon-phonon scattering. q is the heat flux through the lattice and G is the thermal conductance between the material sample and the substrate. Γ-optical phonons (or zone-center optical phonons) are singled out in this work. The atomic structure in this figure is generated from a toolkit of the Materials Project [20,21].

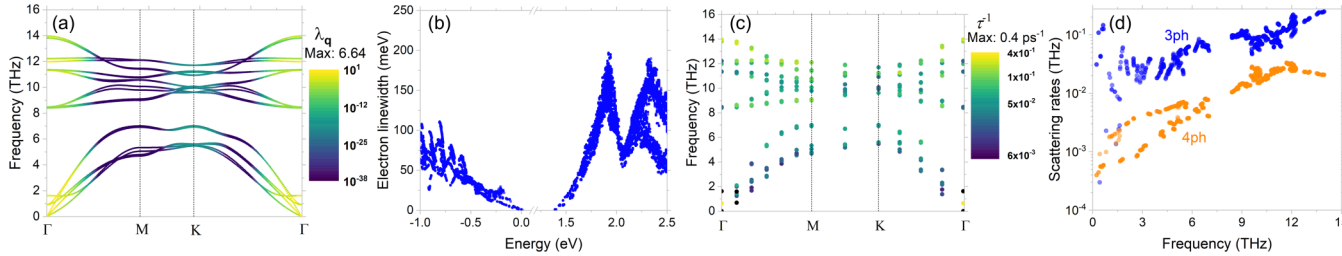

FIG. 2. Electron-phonon coupling and phonon transport properties at 300 K in bulk MoS_2. (a) The electron-phonon coupling strength $\lambda_{\mathbf{q}}$ and its mapping onto the phonon dispersion curve. (b) Electron linewidth or imaginary part of its self-energy as a function of electron energy. This plot shows the contribution of electron-phonon scattering to the electronic linewidth. (c) Phonon-phonon scattering rates τ^{-1} and its mapping onto the phonon dispersion curve. (d) Anharmonic phonon scattering rates with contributions from three-phonon ($\tau_{3\text{ph}}^{-1}$, blue dots) and four-phonon scatterings ($\tau_{4\text{ph}}^{-1}$, orange dots). In (a) and (c), the contour color-bar levels are in logarithmic scale.

not be sufficient for this particular material. The calculated electron linewidth as a function of the electron energy is also shown in Fig. 2(b). In addition, we also obtain the electron-phonon coupling factor G_{ep} for energy flow from electrons into different phonon groups. As shown by the calculated phonon-phonon scattering rates in Figs. 2(c) and 2(d), optical phonons have higher scattering rates that generally increases with increasing phonon frequency. A detailed analysis into different phonon scattering channels in Fig. 2(d) indicates that four-phonon scatterings ($\tau_{4\text{ph}}^{-1}$) are generally one magnitude lower than their three-phonon counterpart ($\tau_{3\text{ph}}^{-1}$). Thus, in the present work we only calculate phonon coupling factors G_{pp} based on three-phonon scattering rates. In our work, the coupling factors G_{ep} and G_{pp} are all obtained through first-principles calculations.

In previous works [10,13], the standard multitemperature model (MTM) resolves phonons at the polarization level without differentiating phonons from the same branch at different momentum spaces. Based on our modewise scattering rate calculation results for MoS_2, we specify five different equivalent temperatures for electrons, zone-center optical phonons, high-frequency non-zone-center optical phonons, low-frequency non-zone-center optical phonons, and acoustic phonons. In this way, the previous MTM [10,13] is extended to resolve phonons in both energy and momentum spaces. In addition, the energy equation is modified to include a recombination process and hole diffusion for semiconductor systems. We refer to this approach as semiconductor MTM (or SC-MTM),

$$C_{e(h)}\frac{\partial T_{e(h)}}{\partial t} = \nabla(\kappa_{e(h)}\nabla T_{e(h)}) + r_{e(h)}\frac{Q}{h\nu}(h\nu - E_g) - \sum_i G_{e(h)p,i}(T_{e(h)} - T_{p,i}) - \frac{3}{2}k_B T_{e(h)} n_r', \quad (1)$$

where the subscript $e(h)$ represents electrons (holes) and (p, i) represents a certain phonon subgroup, C denotes specific heat, κ is the thermal conductivity, T is temperature and G is the coupling factor for each subgroup, Q is the external energy source, E_g is the band gap, $h\nu$ is the photon energy, $\frac{3}{2}k_B T_{e(h)}$ is the thermal energy electrons (holes) have, and n_r' is the recombination rate. The ratio of effective mass is defined as $r_{e(h)} = \frac{m^*_{r,e(h)}}{m^*_{r,e}+m^*_{r,h}}$. In this formulation, the second term on the right-hand side represents the kinetic energy from photons in excess of the band gap gained by the electron/hole, the third term is the cooling by electron- (hole-)phonon coupling, and the last term represents the thermal energy lost in recombination. Compared to metals, the band gap should be subtracted when determining carrier temperatures.

For each phonon subgroup i, we have

$$C_{p,i}\frac{\partial T_{p,i}}{\partial t} = \nabla(\kappa_{p,i}\nabla T_{p,i}) + G_{e(h)p,i}(T_{e(h)} - T_{p,i}) + G_{pp,i}(T_{\text{lat}} - T_{p,i}) + \dot{q}_i. \quad (2)$$

In particular, we define a lattice reservoir T_{lat} with which all phonon subgroups should exchange energy to satisfy energy conservation: $\sum G_{pp,i}(T_{\text{lat}} - T_{p,i}) = 0$. By doing this, the phonon coupling factors are easily related to the phonon lifetime τ_i under relaxation time approximation (RTA): $G_{pp,i} = \frac{C_{p,i}}{\tau_i}$. Note that $\dot{q}_i$ is the fraction of the total recombination heating $\dot{q}$ that goes to group i and we assume that the entire recombination process is nonradiative. Considering the band gap energy is large compared to the phonon energy, the nonradiative recombination will be a multiphonon process. The most probable process would be depositing the energy to the zone-center optical phonons (detailed discussions on the above reasonings can be found in the Supplemental Material [31]):

$$\dot{q}(x) = \left(E_g + \tfrac{3}{2}k_B T_e\right)n_r'. \quad (3)$$

The energy source Q represents the absorbed Gaussian laser power density in an axisymmetric system and it reads $Q(r, z) = \alpha I(r, z)$, with $I(r, z)$ being the laser intensity profile [32],

$$I(r, z) = \frac{2P(1-R)}{\pi w(z)^2}e^{-\frac{2r^2}{w(z)^2}-\alpha z}. \quad (4)$$

In the above equation, P denotes the laser power, R is the reflectance, α is the absorption coefficients of the sample, and $w(z)$ is the laser beam divergence relation at a certain depth z (these parameters are discussed in the Supplemental Material [31]).

The recombination rate can be expressed in relaxation time form $n_r' \approx \frac{n}{\tau_n}$, where τ_n is the carrier recombination lifetime, and n is the excited carrier density. Thus, to solve the extended MTM energy Eqs. (1) and (2), we need to determine the spatial carrier density n by the carrier diffusion equation [33],

$$\frac{\partial n_{e(h)}}{\partial t} = D_{e(h)}\nabla^2 n_{e(h)} + n_g' - n_r', \quad (5)$$

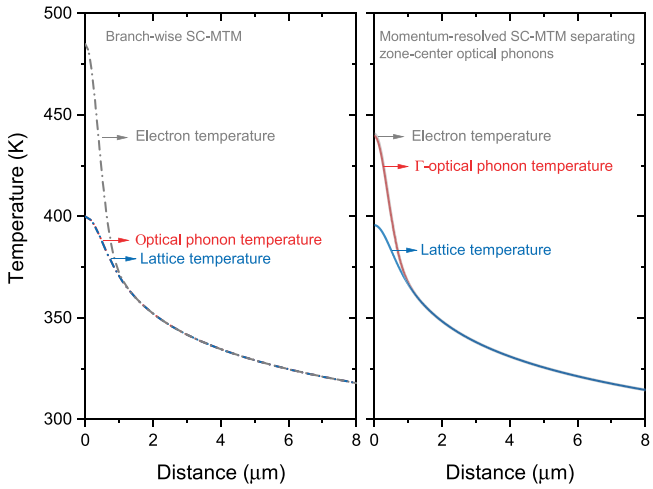

FIG. 3. Extended semiconductor multitemperature model with both energy and momentum resolutions. The x axis of this plot is the distance from the laser spot center. The suspended region of our sample is 15 μm in radius and here we show the localized heating up to 8 μm. The data are calculated under laser irradiation with the Gaussian radius $r = 0.71$ μm and power $P = 2.35$ mW.

where $D_{e(h)}$ is the diffusion coefficient of carriers, and $n'_g = \frac{Q}{h\nu}$ is the carrier generation rate. We estimate that electrons and holes in our material system have similar diffusion coefficients and effective masses [34,35] and similar behaviors. Thus, in this specific work the solution of the above equations can be simplified to have just one equation where electrons and holes are lumped [31]. Details and some discussions on electron/hole diffusion, the carrier density profile, and Fermi level are also presented in the Supplemental Material [31], which includes Refs. [34–39]. Equations (1), (2), and (5) are solved numerically in real space with axisymmetric boundary conditions using finite-element methods in COMSOL MULTIPHYSICS [40].

Figure 3 compares the calculation results from the branchwise SC-MTM and the present momentum-resolved SC-MTM model. The branchwise MTM assigns two different average phonon temperatures, one for the optical branches and the other for the acoustical branches. While the previous branchwise MTM can reveal phonon nonequilibrium in metals and graphene [10,13–15], its semiconductor modification cannot produce any observable phonon nonequilibrium in bulk MoS_2, as shown in Fig. 3(a). In comparison, the momentum-resolved SC-MTM model reveals apparently higher temperatures for the zone-center optical phonons than $T_{\rm lat}$. This result suggests that the zone-center optical phonons in bulk MoS_2 are coupled preferentially to electrons and are not effectively cooled down by the lattice. Based on this result, phonon nonequilibrium in laser-irradiated MoS_2 mainly occurs in the momentum space between the zone-center modes and other modes, instead of between phonons of different polarizations. Essentially, the energy flow bottleneck is mainly in the momentum space instead of across the different energy ranges or polarizations. The electron temperature (shown in gray lines) is also higher in the eyes of branch-wise SC-MTM than predicted by momentum-resolved SC-MTM. Electrons

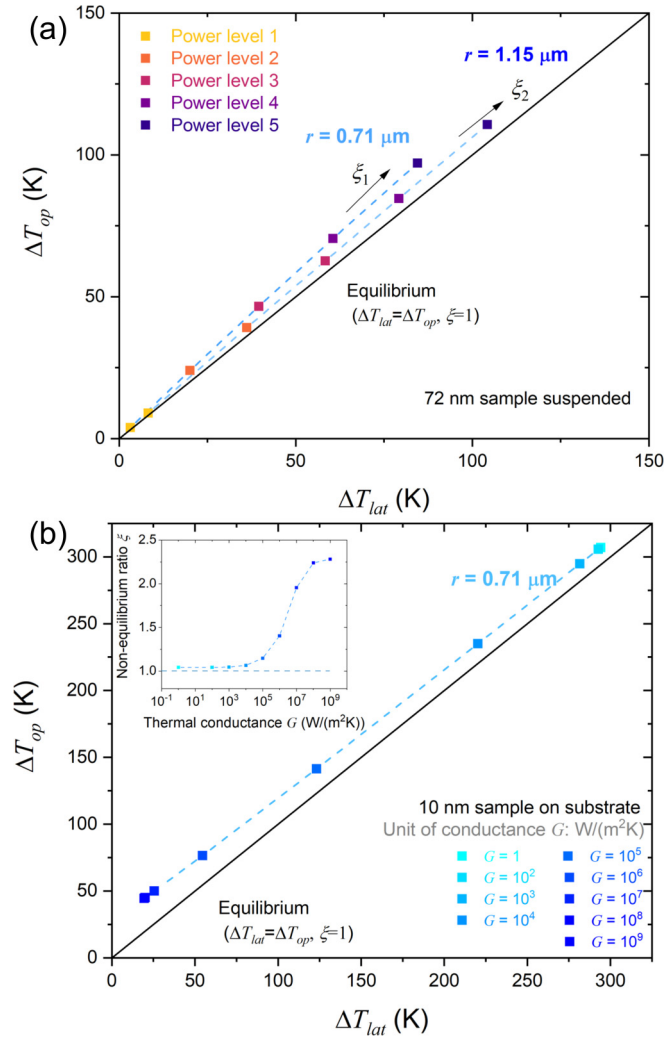

FIG. 4. Effect of laser spot size and substrate coupling on the nonequilibrium ratio ξ. ξ is interpreted as the slope of line passing through the origin. (a) The hottest phonon temperature rise with respect to the lattice temperature rise at increasing laser power levels 1–5 for suspended MoS_2 that has a thickness of 72 nm. The slope yields ξ, and r is the laser spot size. The solid black line with unity slope indicates the equilibrium state. (b) The hottest phonon temperature rise with respect to the lattice temperature rise for supported MoS_2 that has a thickness of 10 nm at different thermal interface conductances, a fixed laser radius $r = 0.71$ μm, and power $P = 2.35$ mW. The inset shows the calculated nonequilibrium ratio ξ as a function of conductance G_i.

are at equilibrium with zone-center optical phonons as revealed by our extended model.

We define a nonequilibrium ratio as $\xi = \Delta T_{\rm h}/\Delta T_{\rm lat}$ between the temperature rise of the hottest group ($\Delta T_{\rm h}$) and that of the lattice ($\Delta T_{\rm lat}$). In the case of bulk MoS_2, $\Delta T_{\rm h}$ is the temperature rise ($\Delta T_{\rm op}$) of the zone-center optical phonons. In Fig. 4(a) that has accounted for the effect of the laser-induced temperature rise, this ratio is obtained as the slope of the calculated $\Delta T_{\rm op}$ vs $\Delta T_{\rm lat}$ at different laser powers and each laser spot size for a suspended sample. Though the change of nonequilibrium with respect to laser power is marginal in this system [indicated by the almost linear relation in Fig. 4(a)],

the numerical solutions do show a decrease of nonequilibrium with a higher laser power level. This power dependence is in agreement with and explained in a prior study of graphene [11]. Our simulated nonequilibrium ratio under the same experimental condition is 1.15 when $r = 0.71$ μm, in good agreement with Ref. [17]. Compared to the degree of phonon nonequilibrium observed in graphene ($\xi > 2$) [10,11], this reduced ratio is understandable as bulk MoS_2 has lower thermal conductivity and generally stronger phonon scatterings than graphene. Additionally, the ZA mode in graphene couples weakly with other phonon modes and essentially cools down the lattice. When the Gaussian laser beam radius decreases from 1.15 to 0.71 μm and approaches the thermalization length of hot zone-center phonons, the zone-center phonons are not able to thermalize with the lattice within the laser spot, resulting in a higher ξ at a smaller laser spot size.

We further examine the effect of substrate phonon coupling on the nonequilibrium ratio, as the findings will have practical implications for electronic devices made with supported MoS_2 layers [41]. Thus, we choose a model sample with a thickness of 10 nm on the SiO_2 substrate in this case. Acoustic phonon modes of SiO_2 lie in the same frequency range as MoS_2 (∼5 THz). Since high-group-velocity acoustic phonons usually make the dominant contribution to the interface conductance and considering the fact that the low-frequency optical phonons in bulk MoS_2 are in near equilibrium with the lattice, in our model the interface conductance term is only added to the acoustic phonon group, where the energy outflow to the substrate is proportional to the temperature difference between the acoustic group (p, a) and the substrate (T_{sub}):

$$C_{p,a}\frac{\partial T_{p,a}}{\partial t} = \nabla(\kappa_{p,a}\nabla T_{p,a}) + G_{ep,a}(T_e - T_{p,a}) + G_{pp,a}(T_{\text{lat}} - T_{p,a}) - G_i(T_{p,a} - T_{\text{sub}}). \quad (6)$$

As shown in Fig. 4(b), an increase in the interface conductance G_i would decrease the overall lattice temperature rise ΔT_{lat} more than ΔT_{op} for a given laser power level and laser spot size, because ΔT_{lat} is cooled directly by interface heat transport mainly caused by the interface coupling of acoustic phonons. Consequently, the nonequilibrium ratio ξ increases with G_i.

These results show that the conventional phonon branchwise multitemperature model (MTM) revised for semiconductors (SC-MTM) does not yield any observable phonon nonequilibrium in laser-irradiated MoS_2. However, when we extend the model to have both energy and momentum dimensions, a moderate nonequilibrium is produced and can explain the experimental data in Ref. [17]. This implies that thermal equilibrium is well established between phonon groups having different energy states, but not between phonons with different momenta even in the same branch. Only the extended SC-MTM that treats the zone-center phonon separately, while not the conventional phonon branchwise SC-MTM, can predict the phonon nonequilibrium that is observed in concurrent experiments. Based on this finding, whether phonons should be resolved in both energy and momentum space should be based on first-principles calculations of electron-phonon and phonon-phonon interactions. The degree of hot zone-center optical phonons is increased with a reduced laser spot size and substrate coupling of acoustic modes. These findings provide detailed insights on phonon nonequilibrium phenomena in optically or electrically excited functional materials and devices.

X.R., Z.H., and L.S., P.S. were supported by two collaborating Grants (No. 2015946 and No. 2015954) of the U.S. National Science Foundation. Simulations were performed at the Rosen Center for Advanced Computing (RCAC) of Purdue University.

[1] P. B. Allen, Theory of Thermal Relaxation of Electrons in Metals, Phys. Rev. Lett. **59**, 1460 (1987).
[2] S. Sadasivam, M. K. Y. Chan, and P. Darancet, Theory of Thermal Relaxation of Electrons in Semiconductors, Phys. Rev. Lett. **119**, 136602 (2017).
[3] J. Urayama, T. B. Norris, J. Singh, and P. Bhattacharya, Observation of Phonon Bottleneck in Quantum Dot Electronic Relaxation, Phys. Rev. Lett. **86**, 4930 (2001).
[4] A. J. Nozik, Quantum dot solar cells, Phys. E **14**, 115 (2002).
[5] J. Yang, X. Wen, H. Xia, R. Sheng, Q. Ma, J. Kim, P. Tapping, T. Harada, T. W. Kee, F. Huang *et al.*, Acoustic-optical phonon up-conversion and hot-phonon bottleneck in lead-halide perovskites, Nat. Commun. **8**, 14120 (2017).
[6] T. Qiu and C. Tien, Short-pulse laser heating on metals, Int. J. Heat Mass Transfer **35**, 719 (1992).
[7] A. Majumdar and P. Reddy, Role of electron-phonon coupling in thermal conductance of metal-nonmetal interfaces, Appl. Phys. Lett. **84**, 4768 (2004).
[8] L. Waldecker, R. Bertoni, H. Hübener, T. Brumme, T. Vasileiadis, D. Zahn, A. Rubio, and R. Ernstorfer, Momentum-Resolved View of Electron-Phonon Coupling in Multilayer WSe_2, Phys. Rev. Lett. **119**, 036803 (2017).
[9] T. Shin, S. W. Teitelbaum, J. Wolfson, M. Kandyla, and K. A. Nelson, Extended two-temperature model for ultrafast thermal response of band gap materials upon impulsive optical excitation, J. Chem. Phys. **143**, 194705 (2015).
[10] A. K. Vallabhaneni, D. Singh, H. Bao, J. Murthy, and X. Ruan, Reliability of Raman measurements of thermal conductivity of single-layer graphene due to selective electron-phonon coupling: A first-principles study, Phys. Rev. B **93**, 125432 (2016).
[11] S. Sullivan, A. Vallabhaneni, I. Kholmanov, X. Ruan, J. Murthy, and L. Shi, Optical generation and detection of local nonequilibrium phonons in suspended graphene, Nano Lett. **17**, 2049 (2017).
[12] Y. Wang and X. Xu, Molecular dynamics studies of ultrafast laser-induced nonthermal melting, Appl. Phys. A **110**, 617 (2013).
[13] Z. Lu, A. Vallabhaneni, B. Cao, and X. Ruan, Phonon branch-resolved electron-phonon coupling and the multitemperature model, Phys. Rev. B **98**, 134309 (2018).
[14] L. Waldecker, R. Bertoni, R. Ernstorfer, and J. Vorberger, Electron-Phonon Coupling and Energy Flow in a Simple Metal beyond the Two-Temperature Approximation, Phys. Rev. X **6**, 021003 (2016).

[15] M. An, Q. Song, X. Yu, H. Meng, D. Ma, R. Li, Z. Jin, B. Huang, and N. Yang, Generalized two-temperature model for coupled phonons in nanosized graphene, Nano Lett. **17**, 5805 (2017).

[16] H. Zobeiri, N. Hunter, N. V. Velson, C. Deng, Q. Zhang, and X. Wang, Interfacial thermal resistance between nm-thick MoS_2 and quartz substrate: A critical revisit under phonon mode-wide thermal non-equilibrium, Nano Energy **89**, 106364 (2021).

[17] P. Sokalski, Z. Han, G. C. Fleming, B. Smith, S. E. Sullivan, R. Huang, X. Ruan, and L. Shi, Effects of hot phonons and thermal stress in micro-Raman spectra of molybdenum disulfide, Appl. Phys. Lett. **121**, 182202 (2022).

[18] F. Caruso, Nonequilibrium lattice dynamics in monolayer MoS_2, J. Phys. Chem. Lett. **12**, 1734 (2021).

[19] D. Novko, F. Caruso, C. Draxl, and E. Cappelluti, Ultrafast Hot Phonon Dynamics in MgB_2 Driven by Anisotropic Electron-Phonon Coupling, Phys. Rev. Lett. **124**, 077001 (2020).

[20] A. Jain, S. P. Ong, G. Hautier, W. Chen, W. D. Richards, S. Dacek, S. Cholia, D. Gunter, D. Skinner, G. Ceder, and K. A. Persson, The Materials Project: A materials genome approach to accelerating materials innovation, APL Mater. **1**, 011002 (2013).

[21] S. P. Ong, W. D. Richards, A. Jain, G. Hautier, M. Kocher, S. Cholia, D. Gunter, V. L. Chevrier, K. A. Persson, and G. Ceder, Python Materials Genomics (pymatgen): A robust, open-source python library for materials analysis, Comput. Mater. Sci. **68**, 314 (2013).

[22] A. Othonos, Probing ultrafast carrier and phonon dynamics in semiconductors, J. Appl. Phys. **83**, 1789 (1998).

[23] P. Venkat and T. Otobe, Three-temperature modeling of laser-induced damage process in silicon, Appl. Phys. Express **15**, 041008 (2022).

[24] J. H. Seol, I. Jo, A. L. Moore, L. Lindsay, Z. H. Aitken, M. T. Pettes, X. Li, Z. Yao, R. Huang, D. Broido, N. Mingo, R. S. Ruoff, and L. Shi, Two-dimensional phonon transport in supported graphene, Science **328**, 213 (2010).

[25] G. Kresse and J. Hafner, *Ab initio* molecular dynamics for liquid metals, Phys. Rev. B **47**, 558 (1993).

[26] A. Togo and I. Tanaka, First principles phonon calculations in materials science, Scr. Mater. **108**, 1 (2015).

[27] W. Li, J. Carrete, N. A. Katcho, and N. Mingo, ShengBTE: A solver of the Boltzmann transport equation for phonons, Comput. Phys. Commun. **185**, 1747 (2014).

[28] Z. Han, X. Yang, W. Li, T. Feng, and X. Ruan, FourPhonon: An extension module to ShengBTE for computing four-phonon scattering rates and thermal conductivity, Comput. Phys. Commun. **270**, 108179 (2022).

[29] P. Giannozzi, S. Baroni, N. Bonini, M. Calandra, R. Car, C. Cavazzoni, D. Ceresoli, G. L. Chiarotti, M. Cococcioni, I. Dabo, A. D. Corso, S. de Gironcoli, S. Fabris, G. Fratesi, R. Gebauer, U. Gerstmann, C. Gougoussis, A. Kokalj, M. Lazzeri, L. Martin-Samos *et al.*, QUANTUM ESPRESSO: A modular and open-source software project for quantum simulations of materials, J. Phys.: Condens. Matter **21**, 395502 (2009).

[30] S. Poncé, E. Margine, C. Verdi, and F. Giustino, EPW: Electron-phonon coupling, transport and superconducting properties using maximally localized Wannier functions, Comput. Phys. Commun. **209**, 116 (2016).

[31] See Supplemental Material at http://link.aps.org/supplemental/10.1103/PhysRevB.107.L041407 for computational details and laser parameters.

[32] K. An, K. S. Olsson, A. Weathers, S. Sullivan, X. Chen, X. Li, L. G. Marshall, X. Ma, N. Klimovich, J. Zhou, L. Shi, and X. Li, Magnons and Phonons Optically Driven out of Local Equilibrium in a Magnetic Insulator, Phys. Rev. Lett. **117**, 107202 (2016).

[33] B. G. Streetman and S. K. Banerjee, *Solid State Electronic Devices* (Pearson Education, London, 1975).

[34] W. Bao, X. Cai, D. Kim, K. Sridhara, and M. S. Fuhrer, High mobility ambipolar MoS_2 field-effect transistors: Substrate and dielectric effects, Appl. Phys. Lett. **102**, 042104 (2013).

[35] T. Cheiwchanchamnangij and W. R. L. Lambrecht, Quasiparticle band structure calculation of monolayer, bilayer, and bulk MoS_2, Phys. Rev. B **85**, 205302 (2012).

[36] N. Kumar, J. He, D. He, Y. Wang, and H. Zhao, Charge carrier dynamics in bulk MoS_2 crystal studied by transient absorption microscopy, J. Appl. Phys. **113**, 133702 (2013).

[37] W. J. Yu, Q. A. Vu, H. Oh, H. G. Nam, H. Zhou, S. Cha, J.-Y. Kim, A. Carvalho, M. Jeong, H. Choi, A. H. C. Neto, Y. H. Lee, and X. Duan, Unusually efficient photocurrent extraction in monolayer van der Waals heterostructure by tunnelling through discretized barriers, Nat. Commun. **7**, 13278 (2016).

[38] P. Yuan, J. Liu, R. Wang, and X. Wang, The hot carrier diffusion coefficient of sub-10 nm virgin MoS_2: uncovered by non-contact optical probing, Nanoscale **9**, 6808 (2017).

[39] R. Dagan, Y. Vaknin, A. Henning, J. Y. Shang, L. J. Lauhon, and Y. Rosenwaks, Two-dimensional charge carrier distribution in MoS_2 monolayer and multilayers, Appl. Phys. Lett. **114**, 101602 (2019).

[40] COMSOL, Inc, COMSOL Multiphysics v. 5.6., www.comsol.com.

[41] W. Zheng, C. J. McClellan, E. Pop, and Y. K. Koh, Nonequilibrium phonon thermal resistance at MoS_2/oxide and graphene/oxide interfaces, ACS Appl. Mater. Interfaces **14**, 22372 (2022).